



## Research paper

## Energy flux variations and safety assessment of offshore wind and wave resources during typhoons in the northern South China Sea

Yi Wen <sup>a,b,1</sup>, Xingkun Xu <sup>b,1</sup>, Takuji Waseda <sup>b</sup>, Pengzhi Lin <sup>c,\*</sup><sup>a</sup> College of Architecture and Environment, Sichuan University, 24, South Section No.1, Yihuan Road, Chengdu, 610065, China<sup>b</sup> Department of Ocean Technology Policy and Environment, Graduate School of Frontier Science, The University of Tokyo, Chiba, Japan<sup>c</sup> State Key Laboratory of Hydraulics and Mountain River Engineering, Sichuan University, 24, South Section No.1, Yihuan Road, Chengdu, 610065, China

## ARTICLE INFO

## ABSTRACT

**Keywords:**  
 Offshore wind energy  
 Wave energy  
 WRF  
 FVCOM-SWAVE  
 Device safety

Extreme ocean conditions during typhoons pose significant challenges to the sustainable utilization of ocean renewable energy. This study focuses on analyzing the wind and sea states within typhoon systems and the variations in offshore wind & wave energy flux during typhoons passing over the northern South China Sea (SCS) from 2000 to 2022. The trajectories and intensities of 769 typhoons in the Western Pacific, along with wind & wave energy flux variations during 155 instances of typhoons making landfall in the SCS, are isolated for comprehensive analysis. Specifically, the safety of energy exploitation during severe typhoon Hato (2017) is assessed considering the local met-ocean condition during typhoon passing and the survival ocean conditions of Offshore Wind Turbines (OWTs) and Wave Energy Converters (WECs). The WRF model and FVCOM-SWAVE model are used to provide necessary winds and waves during the passage of Hato with simulations validated against observations for reliable safety assessments. The results show that, over the past 22 years, the regions spanning from northern Guangdong to the Luzon Strait have been subjected to robust winds and formidable waves. The average values of Wind Power Density (WPD) and Wave Power Flux (WPF) during typhoons have exceeded 1500 W/m<sup>2</sup> and 20 kW/m, respectively. In the Hato typhoon system, the maximum wind speed surpasses 60 m/s, while the significant wave height is about 10 m. Moreover, the survival capabilities of current OWTs (MySE5.5-155, SWT-6.0-154, SWT-7.0-154, SG 8.0-167 DD and D10000-185) and WECs (Sea Power and CycWEC) are assessed, demonstrating their ability to withstand the entire typhoon lifetime. Therefore, OWTs and WECs exhibit robust survival capabilities through comprehensive assessments based on the validated numerical simulation results, facing extreme typhoon conditions.

## 1. Introduction

Ocean renewable energy has become increasingly significant in the quest for clean energy solutions to meeting rising global energy demands and address environmental concerns (P. Patel et al., 2022). Ocean renewable energy includes offshore wind energy, offshore solar energy, wave energy, tidal/ocean current energy and ocean thermal energy, etc. (Harper et al., 2016). Among these, offshore wind and wave energy has become highly efficient way to address the energy and environmental challenges. This is because their high energy flux and widespread availability (Li et al., 2022). Recently, there has been a pronounced attention on enhancing the conversion and adept management of offshore wind and wave energy through Offshore Wind Turbines

(OWTs) and Wave Energy Converters (WECs), due to their capacity to contribute substantially to the electricity supply of coastal cities, islands, and ocean platforms (Kamranzad et al., 2020). However, extreme ocean conditions during typhoons can significantly impact the sustainable utilization of ocean renewable energy by disrupting operations and causing structural damage. Ocean energy conversion devices and Operation and Maintenance (O&M) ships are susceptible to damage when exposed to the formidable forces generated by strong winds and waves during typhoons (Liu et al., 2022). For example, during typhoon Chaba in 2022, the offshore wind turbine installation ship "Fujing 001" in Guangdong was damaged and sank near the typhoon center (Chen et al., 2024).

The vulnerability is particularly relevant to China, whose

\* Corresponding author.

E-mail address: [cvelinpz@scu.edu.cn](mailto:cvelinpz@scu.edu.cn) (P. Lin).

<sup>1</sup> Equal Contribution.

commitment to achieving carbon neutrality by 2060, following the Paris Agreement in 2016 (Wei et al., 2022), underscoring the importance of offshore wind and wave energy development. Current studies indicate the abundance of offshore wind and wave energy resources, particularly in the South China Sea's (SCS) nearshore areas (Wen et al., 2022), with Guangdong Province at the forefront of initial development (IEA-OES, 2022). In addition, the southeast waters of Taiwan show abundant wave energy according to the finding of Shih et al. (2018) and Su et al. (2018). However, SCS is highly susceptible to typhoons, given its status as a major western Pacific typhoon development area, experiencing numerous typhoons each year (Li et al., 2020). Recent study has revealed a noticeable and increasing trend in wind speed and significant wave height on a global and regional scale (Chen, 2024). However, it is expected that the occurrence of tropical cyclones would either decline or stay relatively stable (Walsh et al., 2016). In particular, the occurrence of high-intensity typhoons is increasing in the eastern and central parts of North Pacific (Yoshida et al., 2017). Low-intensity typhoons may provide favorable conditions for maximum energy generation, however, severe weather conditions could potentially threaten marine equipment (i.e., OWTs and WECs) safety near typhoon track (Li et al., 2020).

Current studies of typhoon mainly focus on the ocean dynamic and energy processes, coastal flooding, berthing capacity, design wave conditions and wave energy variation, etc. Loy et al. investigated the oceanic response to the atmospheric forcing in the coastal areas of the Philippines and Vietnam during Durian (2006) and this model's preliminary research intends to offer some insightful information (Loy et al., 2014). Wang et al. examined the characteristics and bearing capability of water surge disasters caused by flood, storm, and combined flood and storm processes in Boao Bay using the MIKE 21 modeling, and the findings demonstrate that the peak water surge level generated by floods and storm surges together is fairly close to the level caused by either flooding or storm surges separately (Wang et al., 2016). Yang et al. examines the physical characteristics and impacts of two super typhoons, Hato (2017) and Mangkhut (2018) based on post-typhoon surveys and numerical modeling. The study investigates the differences in storm surges, wave heights, inundation depths, durations, and flow velocities between the two events (Yang et al., 2019). Hou et al. investigated the wave characteristics of Kanmen Fishing Port under the influence of typhoon Lekima (2019) using the MIKE21 wave model with the Holland wind field model, and assessed the berthing capacity of Kanmen Fishing Port (Hou et al., 2021). Huang et al. analyzed the wave characteristics during typhoon In-Fa (2021) and then looked at the Shengsi fishing port's berthing capacity under various recurrence intervals and route influences (Huang et al., 2023). Sun et al. simulated the storm waves of the 36 typhoon incidents in Manila Bay and depicted how wind-generated waves develop, and dissipate along the coast and offshore, and the results provided design wave conditions for a hypothetical land reclamation project there (Sun et al., 2021). Liu et al. investigated the wave energy during typhoon Lepit (2021) and discussed the differences in wave energy responses between two observational sites. These findings show that the energy density in the two sites has increased from 1.2 to 4.2 kW/m to 5.9–9.5 kW/m, and wave power generation efficiency can reach 100% during this period (Liu et al., 2022).

Although those studies have been conducted to investigate the process and influence during typhoons, the research on wind and wave energy flux variation in the whole area impacted by typhoons is still insufficient. Moreover, the safety assessment of offshore wind and wave energy utilization based on real met-ocean condition during typhoon passing and survival ocean conditions of OWTs and WECs are currently limited. In this work, we investigated offshore wind energy and wave energy flux variations and provided safety assessment based on the operational parameters of marine energy devices at extreme winds and waves. To do so, we analyze the characteristics of typhoons and offshore wind & wave energy flux variation during tropical cyclone passing over 2000–2022 in the northern SCS and conduct an accurate hindcast for

typhoon Hato (2017) through high-resolution numerical models. Based on simulation results, we analyze the extreme wind and wave field development process during typhoon Hato. As such, the survival capability of specific OWTs and WECs can be assessed. Therefore, we provided a meaningful reference to the safe and effective utilizations of wind and wave energy and guidance for the design and/or selections of OWT and WEC in this area.

## 2. Typhoons data analysis

### 2.1. The trajectory and intensity of typhoons over 2000–2022

Typhoons that affect China mainly come from the Pacific Ocean and SCS. To investigate the generation and development characteristics of typhoons that affect China, we analyzed the trajectories and intensities of 769 typhoons to investigate their generation and development characteristics in China. Our analysis, depicted in Fig. 1, included typhoons in the Western Pacific and SCS regions from 2000 to 2022, using data sourced from the China Meteorological Administration (CMA) for reliability (Weather China). According to the National Standards for Tropical Cyclone Levels GBT 19201-2006 from CMA (Weather China), typhoons are divided into six levels based on the maximum wind speed on the ground near the center, i.e., Super Typhoon (Super TY), Strong Typhoon (STY), Typhoon (TY), Strong Tropical Storm (STS), Tropical Storm (TS), and Tropical Depression (TD). The wind speed range for different levels is shown in Fig. 1. As shown in Fig. 1, recurrent strong storm trajectories in specific regions result in distinct color patterns over time: intense red hues in the Western Pacific near the Philippines, indicative of numerous Super TY; shades of orange and yellow in the south and southeast China seas, signaling frequent passage of STY and TY. The SCS is the main development area for typhoons in the Western Pacific, hence, it is necessary to investigate the offshore wind and wave energy flux variations during typhoons.

Figs. 2–5 show the trends of maximum Wind Speed (WSP) and significant wave height (Hs) in SCS over last 22 years. The wind and wave data during typhoons are separated from the ERA5 (fifth-generation European Center for Medium-Range Weather Forecasts atmospheric reanalysis) data (Hersbach et al., 2020). For the initial period spanning 2000 to 2012, we observed a notable increase in WSP, with a rise of approximately 4.5 m/s. This indicates a corresponding increase in typhoon intensities during this timeframe. Conversely, from 2012 to 2022, there was a decrease in WSP by approximately 2.5 m/s, as depicted in Fig. 2. The average maximum WSP over the entire period is approximately 19.5 m/s, as shown in Fig. 3. Similarly, the maximum Hs exhibited a similar trend, increasing by around 1.2 m from 2000 to 2012 and decreasing by approximately 0.5 m from 2012 to 2022, as illustrated in Fig. 4. The average maximum Hs over the entire period is

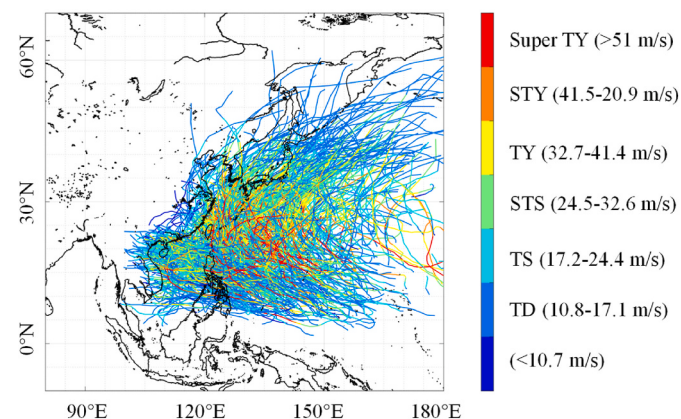


**Fig. 1.** The intensity and trajectory of typhoon occurred in the Western Pacific over 2000–2022, the intensity and trajectory information is from the CMA.

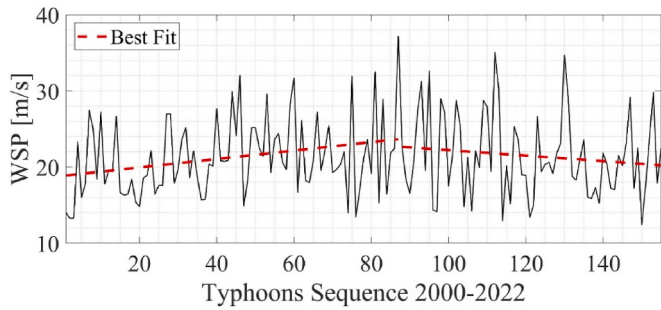


**Fig. 2.** The tendency of maximum 100-m wind speed for 155 typhoons from 2000 to 2022.

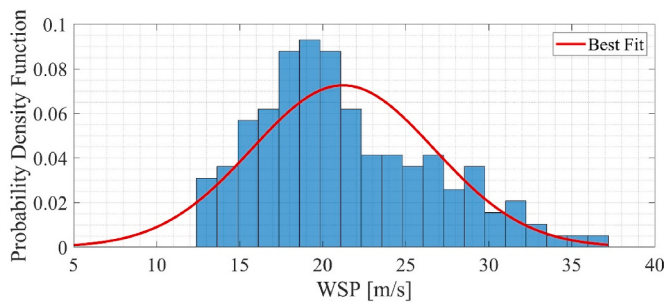


**Fig. 3.** The probability density function of the maximum 100-m wind speed for 155 typhoons from 2000 to 2022.

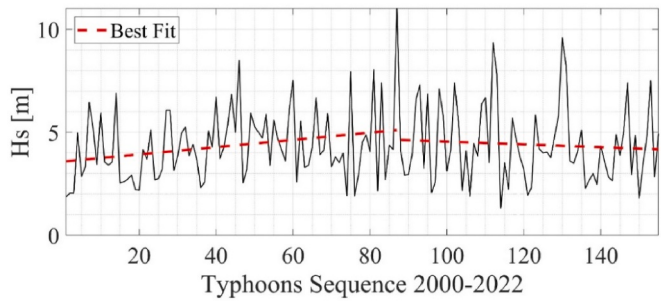


**Fig. 4.** The tendency of the maximum significant wave height for 155 typhoons from 2000 to 2022.

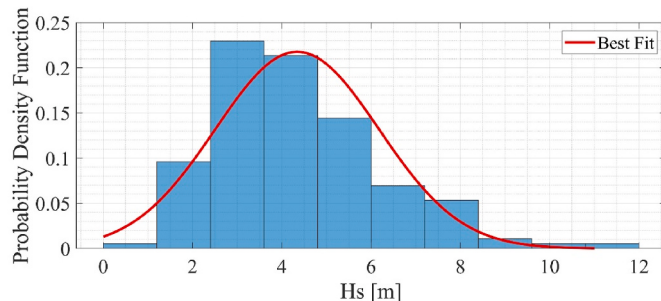


**Fig. 5.** The probability density function of the maximum significant wave height for 155 typhoons from 2000 to 2022.

approximately 3 m, as depicted in Fig. 5.

The evolution, therefore, in met-ocean conditions during typhoon passages in the SCS over the past two decades is dynamic. The observed fluctuations in wind speed and wave height carry significant implications for the safety and sustainability of ocean renewable energy

exploitation in the studied regions. With the heightened intensity of typhoons, it becomes critical to correspondingly elevate the cutoff and/or survival power rates for OWTs and WECs to ensure their safety and stability. However, while the average intensities of typhoons may decrease based on the local wind speed and significant wave height as depicted in Figs. 2 and 4, it does not automatically imply that the cutoff and survival rates should be negatively adjusted accordingly. This is because, in addition to the tendency of the typhoons' individual intensity, factors such as typhoons' occurrence frequency, the possibilities of short-time rapid intensification and long-term climate may also affect the evolution of regional met-ocean conditions (Yao, 2021). These factors need to be included into the design and operation of offshore energy infrastructure, ensuring resilience against changing environmental conditions and enhancing long-term sustainability.

## 2.2. Offshore wind and wave energy flux variations

Among the complete dataset of typhoons in the Pacific Ocean and the SCS, we isolated 155 instances where typhoons made landfall in the SCS for further analysis. For concurrent instantaneous wind speed at a 100-m altitude,  $H_s$ , and peak wave period ( $T_p$ ) during the passage of the 155 selected typhoons, we employed the wind and wave data from ERA5 spanning the years 2000–2022 (Hersbach et al., 2020). The reanalysis data, acquired at hourly intervals, exhibited a spatial resolution of 0.25° for winds and 0.5° for waves.

Before investigating the offshore wind and wave energy flux variation during 2000–2022, the Wind Power Density (WPD) and Wave Power Flux (WPF) need to be calculated by Eqs. (1) and (2) as follows (Wen et al., 2022; Kamranzad et al., 2021):

$$WPD = \frac{1}{2} \rho_a U^3 \quad (1)$$

where  $\rho_a$  indicates the air density (1.225 kg/m³ in this study), and  $U$  is the wind speed at a 100-m altitude.

$$WPF = 0.49 H_s^2 T_e \quad (2)$$

where  $H_s$  and  $T_e$  presents the significant wave height and energy period, respectively. Since the wave period provided by the ERA5 is the  $T_p$ . The relation between  $T_e$  and  $T_p$  can be expressed as:

$$T_e = \alpha T_p \quad (3)$$

where  $\alpha$  is determined by the wave spectrum's form (Li et al., 2022), and  $\alpha = 0.9$  is applied in this study, assuming that the sea state in the research region can be represented by a standard JONSWAP spectrum (Hasselmann et al., 1973).

Fig. 6 present a comprehensive spatial distribution of atmospheric and ocean wave conditions and energy flux for typhoons occurring in the SCS from 2000 to 2022. We observe that the significant wave height is highly consistent with the winds. The wind and wave energy resources in the northern SCS experience considerable impacts of typhoons. Specifically, during typhoons, the strongest states of the waves and winds occurred along the trajectories of the typhoons. The higher frequency of typhoon occurrences around southern Guangdong and the Luzon Strait, irrespective of their eventual landfall destinations. This means that the northern SCS is highly susceptible to typhoons. According to Fig. 6, we observe that the spatial distribution of the WPD and WPF are highly consistent with that of the wind speed and significant wave height, respectively. As the wind and wave energy are in line with the met-ocean conditions, the maximum of WPD and WPF occurs in the areas between northern Guangdong and the Luzon Strait, with the mean values larger than 1500 W/m² and 20 kW/m of WPD and WPF, respectively. However, the average WPD and WPF in summer without non-typhoon conditions are nearly 600–800 W/m² and 4–10 kW/m, respectively (Refs (Li et al., 2022; Wen et al., 2022)). There are significant enhancements in WPF and WPD during typhoons. In contrast with the wind energy, the

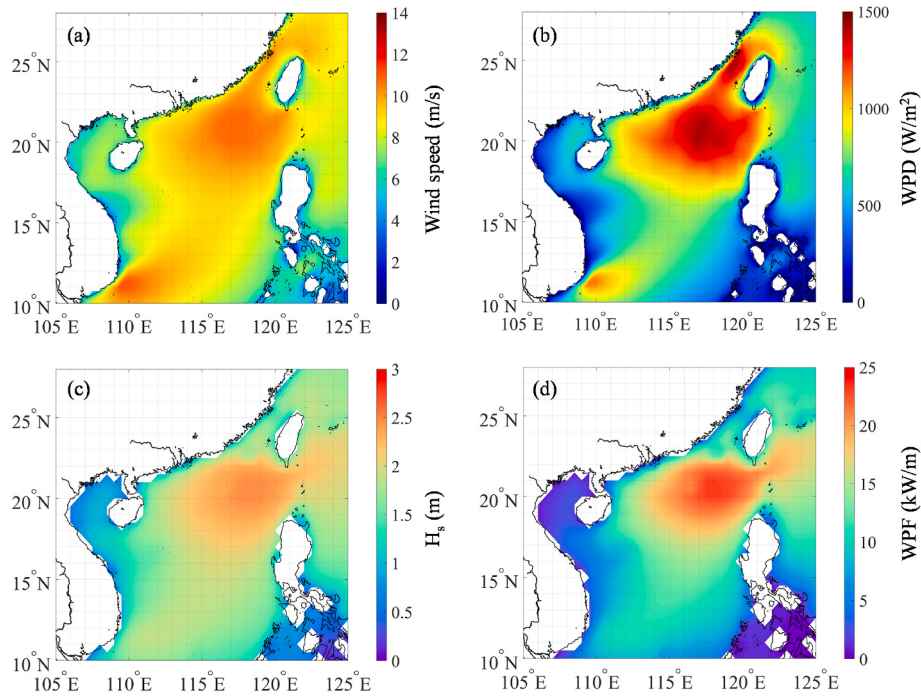


**Fig. 6.** The spatial distribution of (a) average wind speed, (b) WPD, (c) significant wave height, and (d) WPF during typhoons occurred in SCS from 2000 to 2022.

wave energy is less affected by the typhoons in the region of Taiwan Strait. This is because of the geopotential influence of the Taiwan islands, which restricts local wave development due to limited fetch. This result aligns closely with the findings reported by Li et al. (2022). In addition, Guangdong offshore waters is potential areas for both offshore wind and wave farm development (Wen et al., 2022). Hence, it is crucial to further analyze typhoon-driven extreme ocean conditions and device safety in this area.

### 2.3. Design standards of OWTs and WECs

To assess the safety of wind energy utilization, we investigate the operating status and the safety considerations related to offshore wind energy development involving 10 distinct OWTs. To do so, we assume that the OWTs have been deployed in the SCS. The survival wind speed of the OWTs is presented in Table 1. It is noteworthy that the majority of OWTs can survive when wind speeds exceed 55 m/s, except for the GW 171/6450 which can only withstand wind speed up to 37.5 m/s. This is the reason why the GW 171/6450 is installed in the nearshore areas of Liaoning and Jiangsu, China, where the occurrence of typhoons is less frequent.

Fig. 7a shows the OWTs' survival wind speed alongside the maximum wind speeds during the lifespan 155 typhoons that occurred in SCS from 2000 to 2022. The wind speed information is from the CMA

(Weather China). It should be noted that the maximum wind speeds of most typhoons are more than 37.5 m/s but less than 55 m/s. Among the typhoons that made landfall in SCS, Hato (2017) is one of the most severe typhoons, with a maximum wind speed greater than 50 m/s. In addition, Fig. 7b shows the extreme value analysis using General Extreme Value model, we also observe that the return period of the maximum wind speed associated with typhoon Hato extends to approximately 40 years. This suggests that while Hato may not rank as the most formidable cyclone within the past 22 years, its magnitude notably surpasses that of cyclones with a 20-year return period. As such, Hato could arguably be regarded as one of the most potent cyclones on record.

In contrast with OWTs, 3 different WECs are used to investigate the safety within the context of wave energy development. As with the OWTs, we assume the installation of these WECs in the SCS. The survival wave heights of different WECs are listed in Table 2. In a line with OWTs, this study evaluates the survival ocean condition (i.e., damage susceptibility) of different WECs. The survival wave height, in the design and deployment of WECs, holds critical importance, as exposure to excessively high waves can precipitate structural damage, diminish power output, or lead to the outright failure of the device. It is, however, imperative to note that survival wave height is just one of a multifaceted spectrum of environmental and operational considerations integral to the design of a WEC. Factors, such as wave period, storm currents also play a significant role in determining the feasibility and effectiveness of a specific WEC design. Notably, as most WECs are still in development and/or testing stage and are yet to be applied in commercialization, specific survival wave height data are not available within the technology manuals for many devices. The survival wave height depends on specific design and type of WEC. For example, the point absorber, the submerged Archimedes Waveswing is designed to position under the waves, giving it the unique advantage of avoiding damaging storm forces. Drawing from the provided survival height data for Wavestar C6, SeaPower, and CycWEC, it is evident that the survival wave height may vary within the range of 6–15 m.

**Table 1**

Design survival wind speed of different OWTs<sup>a</sup>.

Design standard (m/s)	37.5	55	59.5	70	77
Types of OWT	GW 171/6450	HTW5.2-136	Repower 5M; U113; W3600-116	MySE5.5-155; SWT-6.0-154; SWT-7.0-154; SG 8.0-167 DD	D10000-185

<sup>a</sup> Data source: Wind Power (Wind Power).

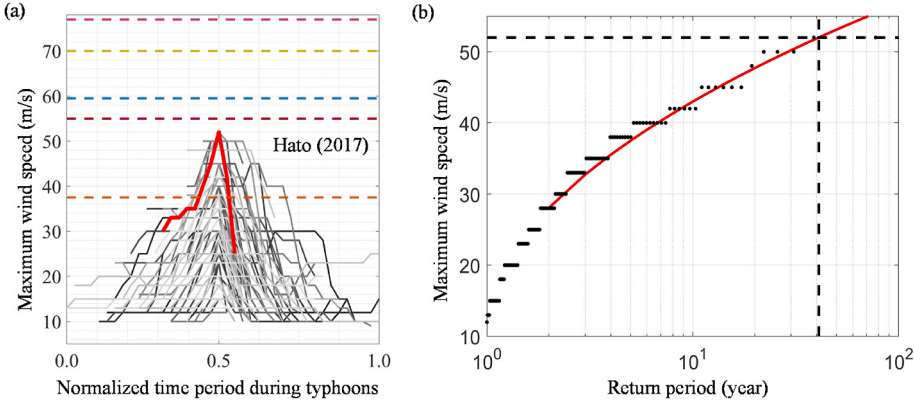


**Fig. 7.** (a) The maximum wind speeds during typhoons' lifespan occurred in SCS from 2000 to 2022, the dashed lines represent the survival wind speeds of different OWTs. The red bold solid line represents the maximum wind speed during the typhoon Hato (2017); (b) The return values of maximum wind speed in different return period. The red solid line is the fitted results, while the dashed lines indicate Hato's maximum wind speed and its corresponding return period.

**Table 2**

Design survival significant wave height of different WECs.

Design standard (m)	6	10.25	15
Types of WEC Refs.	Wavestar C6 (Wavestar)	SeaPower (SEAPOWER)	CycWEC (CycWEC)

### 3. Numerical modeling of extreme sea states during a typical typhoon

According to the previous analysis, Hato (2017) is one of the strongest typhoons to make landfall in SCS in the past 22 years (see Fig. 7). To investigate the sea states under severe weather conditions and the safety of wind and wave energy development, typhoon Hato (2017) is selected to investigate extreme sea states and hence to conduct the individual safety assessment of OWCs and WECs.

#### 3.1. Typhoon Hato (2017)

On August 21, 2017, a tropical depression to the east of Luzon gave rise to Typhoon Hato (Fig. 8). On August 23, 2017, around local time (UTC+8h) 12:50, it rapidly strengthened and landed near Zhuhai, Guangdong, China, as a category of strong typhoon (see Fig. 8). Near its center, the minimum central pressure was 945 hPa, and the estimated maximum sustained wind speed for 10 min was 165 km/h (Macau Meteorological and Geophysical Bureau). The strongest wind recorded since Typhoon Ruby (1964) was reported at Taipa Grande station in Macau, where it reached a maximum gust wind speed of 217.4 km/h (Macau Meteorological and Geophysical Bureau).

#### 3.2. WRF model configurations and validation

We simulated the Typhoon Hato (2017) through using the Weather Research and Forecasting v.4.2 (WRF-ARW, hereafter referred to as WRF) model (Skamarock et al., 2008). WRF is a compressible and non-hydrostatic numerical weather prediction system with a variety of atmospheric physical schemes (Skamarock et al., 2008). In this work, we utilized the Single-Moment 5-class Microphysics scheme (WSM5) (Hong et al., 2004) for the microphysics process, the longwave/short radiation scheme of RRTM for GCMs (RRTMG\_LW/RRTMG\_SW) for the longwave-radiation/shortwave-radiation process (Iacono et al., 2008), the similarity theory (MMS) (Webb, 1970; Dyer and Hicks, 1970; Paulson, 1970) and Yonsei University (YSU) PBL (Hong et al., 2006) for the Surface and Planetary Boundary Layer process, and the 5-layer Thermal Diffusion Scheme (Dudhia, 1996) for the land surface process. The computational domain is shown as Fig. 8a. Due to the limitation of computational resources, the WRF model was run on a 6-km horizontal resolution which is somewhat coarse but still allows for simulating the atmospheric dynamics, specifically within the typhoon scale (Xu et al., 2022). 66 sigma levels in the vertical are adopted, which is sufficiently fine, allowing for simulating atmospheric vertical dynamic processes. We initiated the WRF on 06:00 August 22, 2017 based on the National Centers for Environmental Prediction (NCEP) Global Forecasting System (GFS) data with a horizontal resolution of 0.25° times 0.25° and 6-h interval (CISL RDA). The boundary conditions were derived using the same data (CISL RDA).

We compared WRF simulations of typhoon Hato with observations from three best-track databases, including 1-min, 10-min, and 2-min maximum sustained 10 m wind speeds provided by the Joint Typhoon

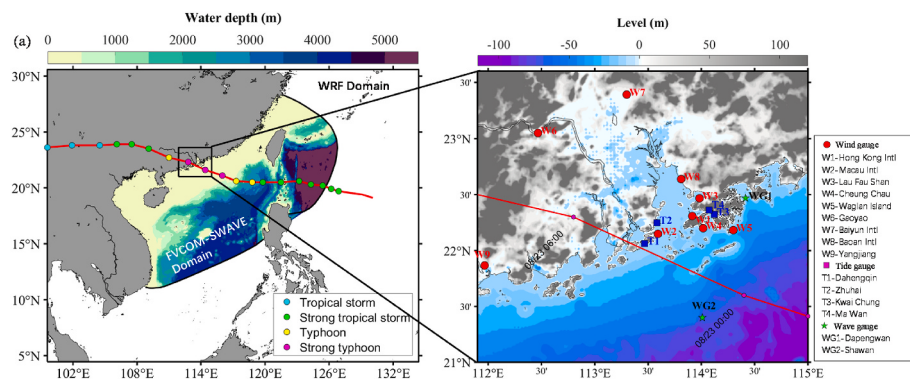


**Fig. 8.** (a) The study areas of different model and the track and intensity of Typhoon Hato (2017); (b) Zoomed into the Pearl River Estuary area and the locations of wind, tide and wave gauges.

Warning Center (JTWC) ([Joint Typhoon Warning Center](#)), Japan Meteorological Agency (JMA) ([Japan Meterological Agency](#)), and CMA ([Weather China](#)), respectively. Fig. 9a shows that, the model successfully reproduced both intensity and trajectory variations. The simulated typhoon intensity is slightly higher than the observation from JMA, the whole process of typhoon Hato is accurately represented in our numerical experiment. A comparison of typhoon trajectory from three best-track databases and that from simulations is shown in Fig. 9b. The trajectories between simulation results and observations are consistent, while the typhoon of WRF modeling moves slightly slower than that from observations. As such, the atmospheric conditions during typhoon Hato (i.e., the typhoon track and intensity) utilized in this work is highly reliable. Fig. 9c presents the winds comparison between the measurements and simulations, specifically in the process of typhoon Hato landfall (cf. Fig. 8b). Winds from the simulations are highly in consistent with the measurements from 9 different gauges, such as the peak wind speed and phase are faithfully reproduced in the modeled wind fields.

To measure the accuracy of the model in simulating wind speed, four error statistical indices, i.e., Bias, Root-mean-square-error (RMSE), Scatter Index (SI), and Pearson correlation coefficient (Cor) are used. The following formulas are utilized in the computation of these indices:

$$Bais = \bar{y} - \bar{x} \quad (4)$$

$$RMSE = \sqrt{\frac{\sum_{i=1}^n (x_i - y_i)^2}{n}} \quad (5)$$

$$SI = \frac{RMSE}{\bar{x}} \quad (6)$$

$$Cor = \frac{\sum_{i=1}^n (x_i - \bar{x})(y_i - \bar{y})}{\sqrt{(\sum_{i=1}^n (x_i - \bar{x})^2)(\sum_{i=1}^n (y_i - \bar{y})^2)}} \quad (7)$$

where  $x_i$  and  $y_i$  indicates the measurement and simulation at  $i$ th time step, respectively;  $\bar{x}$  and  $\bar{y}$  indicates the mean values of measurement and simulation, respectively;  $n$  is the number of total time steps.

**Table 3** presents error indices for wind speed at 9 wind gauge locations. Error indices for wind speed at nine different wind gauge locations are shown in **Table 3**. The bias values demonstrate how well the models can represent the wind speeds at each site, ranging from  $-0.08$  m/s at Yangjiang to  $4.29$  m/s at Macau Intl. All sites have RMSE values smaller than  $6$  m/s, which indicates relatively low overall accuracy. The SI values, which range from  $0.42$  to  $0.64$ , are exceptionally small. The connection between the modeled and observed wind speeds is rather robust, as indicated by the Cor values over  $70\%$  at every location. The validated model is further utilized to force the wave and ocean model

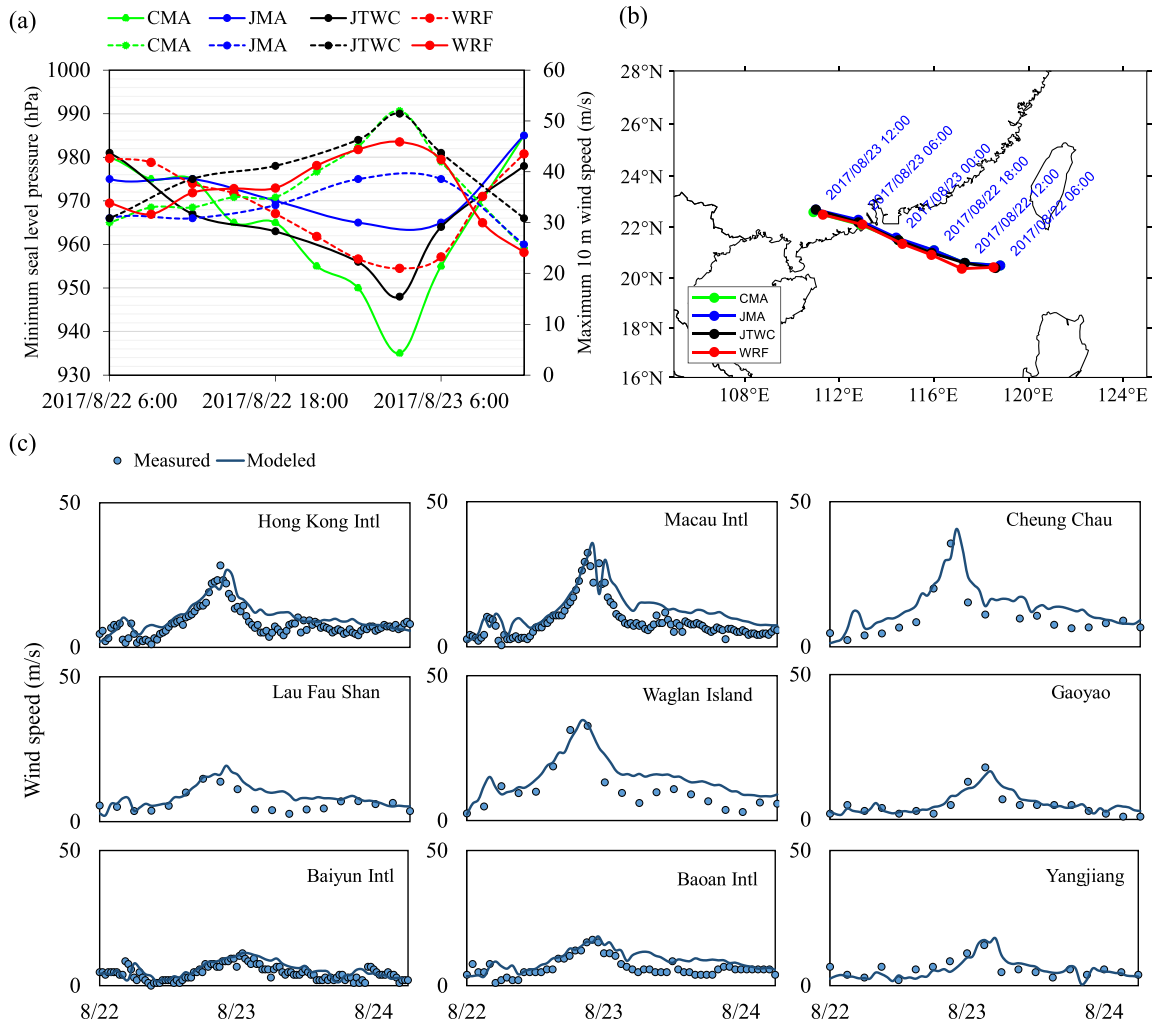


**Fig. 9.** (a) Comparisons of minimum sea level pressure and maximum 10 m wind speed from three best-track databases (i.e., JTWC, JMA, and CMA) and that from WRF simulation; (b) Location and time of the trajectories from observations and that from WRF simulation; (c) Comparisons of measured and simulated 10 m wind speed at different wind gauges during Hato. Locations and names of wind gauges can be checked in Fig. 8b.

**Table 3**

Error indices for wind speed at 9 wind gauge locations.

Sites No.	Sites name	Longitude (°E)	Latitude (°N)	Bias (m/s)	RMSE (m/s)	SI	Cor
W1	Hong Kong Intl	113.915	22.309	2.73	4.09	0.51	0.83
W2	Macau Intl	113.592	22.150	4.29	5.45	0.64	0.86
W3	Cheung Chau	114.017	22.200	3.29	4.76	0.49	0.88
W4	Lau Fau Shan	113.983	22.467	1.80	3.21	0.49	0.73
W5	Waglan Island	114.300	22.183	3.70	5.22	0.48	0.89
W6	Gaoyao	112.467	23.05	0.87	2.18	0.45	0.87
W7	Baiyun Intl	113.299	23.392	1.31	2.41	0.53	0.72
W8	Baoan Intl	113.811	22.639	2.57	3.63	0.54	0.73
W9	Yangjiang	111.967	21.867	-0.08	2.57	0.42	0.72

through providing 10-m wind speed and sea surface pressure.

### 3.3. FVCOM-SWAVE model configurations and validation

To model oceanic responses during Hato passing, the tide-surge-wave coupled model FVCOM-SWAVE is used in this study (Qi et al., 2009). The governing equations of the FVCOM, a finite volume-based three-dimensional (3D) community ocean circulation model, are momentum and continuity equations (Chen et al., 2011). For application in coastal areas with complicated and irregular geometry, the structured-grid surface wave model SWAN (Simulating Waves Nearshore) has been transformed into an unstructured-grid finite-volume version (SWAVE) (Qi et al., 2009). The study area is shown in Fig. 8a. The Surface-water Modeling System (SMS) software is used to generate the model mesh, as shown in Fig. 10. The model mesh is composed of 75,675 triangular elements and 144,164 nodes, and the grid refines mainly in the Hato-impacted areas (i.e., the Pearl River Estuary area). 11-mesh layers are adopted in the vertical direction. The bathymetry dataset from the General Bathymetry Chart of the Oceans (GEBCO) with a spatial resolution of 15 arc-sec is interpolated to the model mesh and used in the model. The refined and smoothed coastline data is from the Global Self-consistent, Hierarchical, High-resolution Geography Database (GSHHG) (Shoreline/Coastline Databases | NCEI). The atmospheric forcing fields from the outputs of the WRF are interpolated to the model mesh and utilized to force the FVCOM-SWAVE model. Along the open ocean boundaries, tide levels are forced by the predicted water levels from TPXO 7.2 dataset with 13 main tide constituents (K1, O1, P1, Q1, M2, S2, N2, K2, M4, MS4, MN4, Mf, Mm) (OSU TPXO), and wave parameters (i.e., significant wave height, peak wave period, and mean wave direction) are from ERA5 reanalysis data (C3S CCCS, 2017). The model starts with hot start mode at the same time of the WRF, and the hot file is from the model output from FVCOM-SWAVE with the same configuration but with an earlier start time (00:00 August 18, 2017) and the forcing wind and pressure fields from the NCEP GFS. The iteration time steps of hydrodynamic model, in this study, is 0.5 s and 5 s for external and internal domain, respectively, and the time step

of wave model is 15 s.

To illustrate the model's accuracy in generating extreme ocean conditions, we compare the modeled water levels and significant wave heights with measurements. To validate the model's performance during Hato, we compare the measured storm tides with the FVCOM-SWAVE simulation results. As shown in Fig. 11, the peak values of storm tide experience a high magnitude of 2.5–3 m at all stations, it is because the storm tide encounters the spring tide. The model can capture both the peak storm tide and the phase well in all stations, indicating that the model performance is acceptable in simulating the hydrodynamic process during Hato. The error indices for water level at four different tide gauge stations are shown in Table 4. The water level bias estimates, which range from 0.08 m to 0.35 m, show slight variations from the measurements. The total accuracy is represented by the RMSE values, which are 0.43 m at T1, 0.40 m at T2, 0.27 m at T3, and 0.47 m at T4. These values are relatively low. The dispersion of the simulated values around the measured values is shown by the SI values. The SI values are 0.30, 0.29, 0.15, and 0.27 at T1, T2, T3, and T4, in that order. These numbers imply that the simulated and measured water levels match quite well. The Cor values of water level—0.91 (T1), 0.97 (T2), and 0.95—are high.

To validate the model's performance in simulating waves, the modeled and measured significant wave heights in two wave stations are compared and presented in Fig. 12. The modeled significant wave heights are comparable with the measured data during typhoon Hato. The modeled peak wave heights are well captured in Dapengwan but a little bit underestimated in Shawan. It is because the wave gauge in Shawan is near to the path of the typhoon center (see Fig. 8b), where the wind field may not be precisely simulated by WRF due to the resolution. Table 5 presents error indices for significant wave height measurements at two wave gauge locations. The two wave gauge locations exhibit positive bias values, with Dapengwan having a bias of 0.75 m and Shawan with a bias of 0.96 m. These values indicate a tendency for the simulations to overestimate the actual significant wave heights at both locations after the typhoon landed. The RMSE values for Dapengwan and Shawan are 0.94 m and 1.42 m, respectively. The two wave

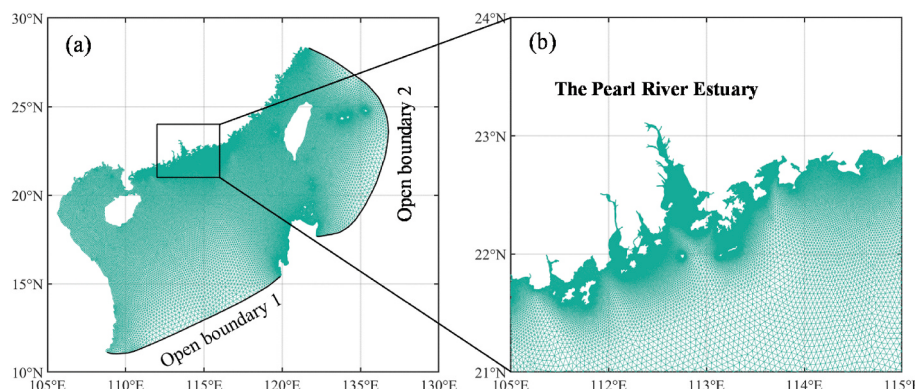
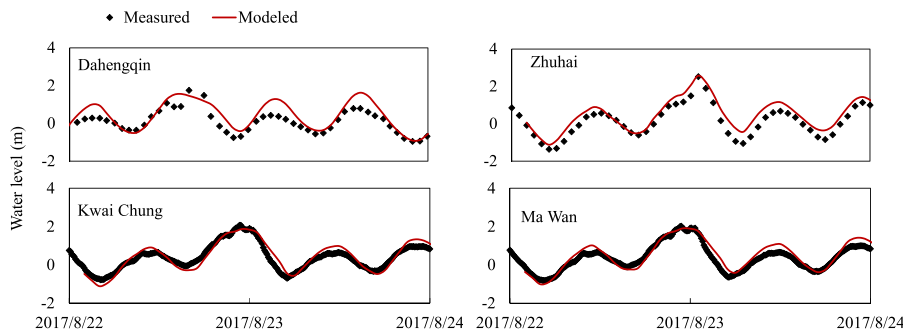


Fig. 10. (a) Model mesh in entire computational domain and (b) zoomed into the Pearl River Estuary area.



**Fig. 11.** Comparisons of modeled water level and measurements of storm tides.

**Table 4**

Error indices for water level at 4 tide gauge locations.

Sites No.	Sites name	Longitude (°E)	Latitude (°N)	Bias (m)	RMSE (m)	SI	Cor
T1	Dahengqin	113.483	22.083	0.27	0.43	0.30	0.91
T2	Zhuhai	113.583	22.250	0.35	0.40	0.29	0.97
T3	Kwai Chung	114.123	22.324	0.08	0.27	0.15	0.95
T4	Ma Wan	114.071	22.364	0.19	0.47	0.27	0.84

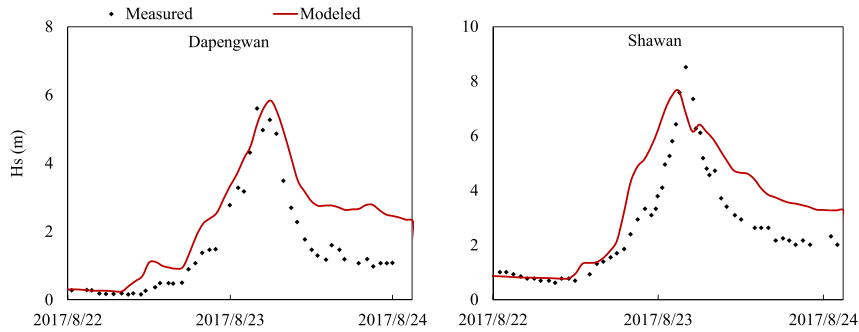


**Fig. 12.** Comparisons of numerically simulated results and measurements of significant wave heights.

**Table 5**

Error indices for significant wave height at 2 wave gauge locations.

Sites No.	Sites name	Longitude (°E)	Latitude (°N)	Bias (m)	RMSE (m)	SI	Cor
WG1	Dapengwan	114.415	22.468	0.75	0.94	0.62	0.93
WG2	Shawan	114.001	21.501	0.96	1.42	0.49	0.85

gauge locations demonstrate SI of less than 0.7, indicating a relatively close agreement between measured and modeled significant wave heights. Both locations show high correlation coefficients, with Dapengwan at 0.93 and Shawan at 0.85, indicating a strong linear relationship between measured and modeled significant wave heights at both locations. Overall, the analysis of error indices presented in Table 5 indicates the accuracy and reliability of significant wave height measurements at the two wave gauge locations.

#### 4. Typical typhoon-driven extreme ocean conditions and device safety considering OWTs and WECs

##### 4.1. Extreme ocean conditions analysis during typhoon Hato

After the WRF and FVCOM-SWAVE are validated, we analyze the typhoon-driven extreme ocean conditions using the model outputs. Wind speed during extreme conditions should be a crucial consideration for offshore wind farm development. Since we focus on offshore energy

during extreme conditions in this study, we exclusively examine the nearshore areas affected by Hato. The upper row of Fig. 13 illustrates the temporal developments of the surface wind speed at 10-m height from 21:00 on August 22 to 06:00 on August 23, 2017 with 3-h time intervals. As shown in the figures, the wind speed reached the highest value at 03:00 on August 23, 2017, before the typhoon's landfall, and then rapidly decreased after the typhoon's landfall. The maximum wind speed (i.e., ~50 m/s) is on the right side of the typhoon track before landfall, which is highly line with the record by CMA (Fig. 7). For offshore wind energy utilization, we pay more attention to the wind field at a hub height, i.e., 100 m in this study (Wen et al., 2021). For this purpose, wind speed at 100-m height is calculated by interpolating from the WRF output at different pressure levels, which correspond to different heights, as shown in the lower row of Fig. 13. According to the figures, the highest wind speed at 100 m is nearly 60 m/s at 00:00 and 03:00 on August 23, respectively. The figures show the similar spatial patterns of the wind field at different heights, while the wind speed at 100-m height is significantly higher than that at 10-m height.

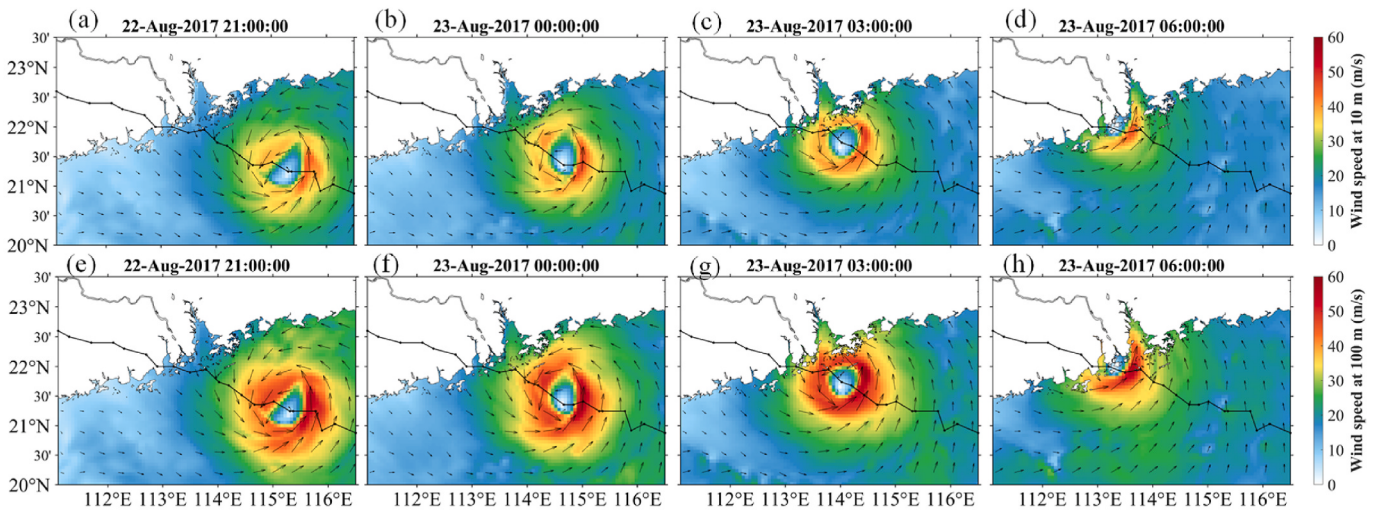


**Fig. 13.** The wind speed and direction at 10 m (a–d) and 100 m height (e–h) from 21:00 on August 22 to 06:00 on August 23 with 3-h time intervals.

Severe ocean states, including wave height and wave period, should be important considerations for marine energy devices' safety. For example, the former studies suggested that the survival wave height of most WECs is from 6 to 10 m (Penalba et al., 2020; Wu et al., 2015). In this study, we investigate the temporal developments of significant wave height and peak wave period from 21:00 on August 22 to 06:00 on August 23, 2017 with 3-h time intervals and present in the upper and lower rows of Fig. 14, respectively. Different from the pattern of wind speed temporal developments, the significant wave height gradually decreases as the typhoon moves to the land because of islands and topography. The maximum significant wave height, around 10 m, exists in the right side of typhoon track at 21:00 on August 22. Meanwhile, the wave height increases much more on the right side than that on the left side of the typhoon track, and it indicates that the cities located on the right side of the typhoon track may be more severely affected. It is interesting that the pattern of temporal developments of peak wave period is similar to that of significant wave height, while the spatial distribution of significant wave height and peak wave period is much different. The peak wave period decrease as the typhoon moves to the land, and the left side of typhoon track experiences a longer wave period than the right side. The maximum peak wave period can reach above 15 s in the left area far away from the typhoon center at 21:00 on August 22. After the typhoon landed, the peak wave period decreased to 5–10 s in

most areas.

#### 4.2. Safety of OWTs and WECs during Hato

To evaluate the safety of offshore wind energy utilization, the

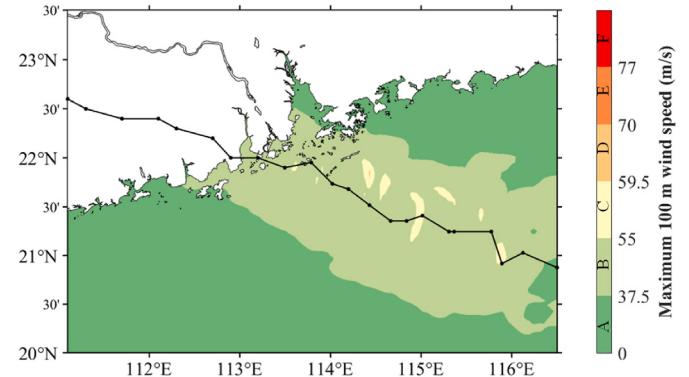


**Fig. 15.** The maximum 100 m wind speed during Hato, color indicates the range of different survival wind speeds for OWTs.

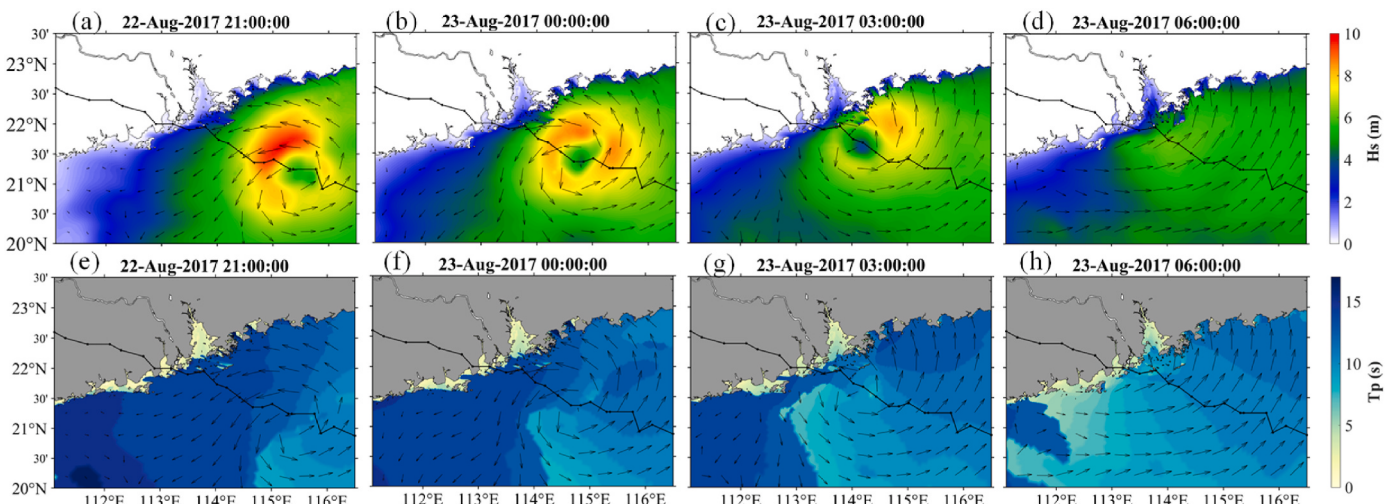


**Fig. 14.** The significant wave height (a–d), and peak wave period (d–h) from 21:00 on August 22 to 06:00 on August 23 with 3-h time intervals.

maximum wind speeds in each grid point during the whole period are calculated and shown in Fig. 15. According to the color of different areas in Fig. 15, we can analyze the risky areas of different OWTs. In the areas C and D, the maximum wind speed is larger than 55 and 59.5 m/s, respectively. The maximum wind speeds in the areas on both sides of the typhoon track (areas D) are larger than 37.5 m/s, which means the GW 171/6450 is likely to be destroyed during Hato if it is installed in these areas. In most areas except areas C and D, the most OWTs except the GW 171/6450 can survive during Hato. The OWTs, GW 171/6450, Repower 5M, HTW5.2-136, U113, and W3600-116 will be likely to be damaged by strong winds in area D. Moreover, the OWTs, MySE5.5-155, SWT-6.0-154, SWT-7.0-154, SG 8.0-167 DD and D10000-185 can survive throughout the whole typhoon period.

To evaluate the safety of wave energy utilization, the maximum significant wave heights in each grid point during the whole period are calculated and shown in Fig. 16. According to the color of different areas in Fig. 16, we can analyze the risky areas of different WECs. The maximum significant wave height in the whole area is less than 10.25 m, and it indicates the CycWEC and SeaPower can survive during Hato if it is installed in any area in Fig. 16. For Wavestar C6, it is likely to be destroyed during Hato if it is installed in area B. It should be noted that the safety of most WECs can't be assessed in this study because most WECs are still in the testing phase.

## 5. Summary and conclusion

In this study, the characteristics of typhoons and the variations in offshore wind and wave energy flux during typhoon passages over the period 2000–2022 in the northern SCS are systematically analyzed. To achieve this objective, the trajectories and intensities of 769 typhoons that occurred in the Western Pacific are considered, and the variations in wind and wave energy flux for 155 instances of typhoon landfalls in the SCS are isolated for in-depth analysis. The safety of energy utilization during typhoon passage was assessed through the investigation of the atmosphere and ocean conditions during typhoon Hato (2017). For this purpose, Two-way coupled wave-current modeling and atmosphere modeling were employed, and simulation results, including typhoon track, intensity, wind speed, wave heights, and water level, were validated against observed data.

Based on the spatial analysis of typhoons in the SCS from 2000 to 2022, high consistency between significant wave height and winds can be observed, with the northern SCS experiencing significant impacts during typhoons. The concentration of typhoon occurrences around the Luzon Strait, regardless of eventual landfall destinations, highlights the heightened susceptibility of the northern SCS, especially the regions between northern Guangdong and the Luzon Strait, to typhoons.

The met-ocean modeling results during typhoon Hato show that the largest 100 m wind speed (nearly 60 m/s) can be found on the right side of the typhoon track at 00:00 and 03:00 on August 23, while the maximum values of significant wave height (around 10 m) and peak wave period (above 15 s) exist in the right side of typhoon Hato and the left area far away from the typhoon center, respectively, at 21:00 on August 22. Moreover, due to swell, the impact areas caused by strong waves are much wider than that caused by strong winds.

The utilization of offshore power generation during the disastrous weather event (e.g., Typhoon Hato) is still a serious challenge. This is because substantial energy devices tend to be turned off for self-preservation and/or damaged by strong waves. Hence, in order to analyze the safety of offshore wind and wave energy equipment during Hato, 10 types of OWT and 3 types of WEC were selected to hypothetically install in the Hato-impacted areas. The investigation showed that the OWT and WEC most likely to be destroyed during Hato are GW 171/6450 and Wavestar C6, respectively. The OWTs, MySE5.5-155, SWT-6.0-154, SWT-7.0-154, SG 8.0-167 DD and D10000-185, and WECs, Sea Power and CycWEC, can survive throughout the whole period of Hato.

As the complicated physics and processes within the typhoon system

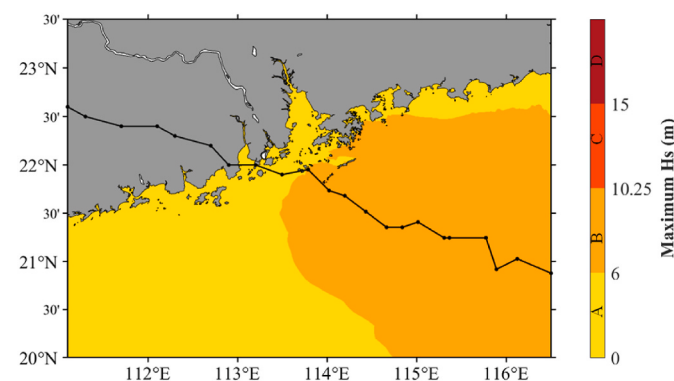


**Fig. 16.** The maximum significant wave height during Hato, color indicates the range of different survival significant wave heights for WECs.

(i.e., trajectories, strength variations, coastline water depth, etc.), substantial cases and subsequent studies are needed to generalize the conclusions in this study. We, however, noted that this study produced a significant theoretical base and reliable practical guidance for future conductions of offshore wind and wave farm projects in this area.

## CRediT authorship contribution statement

**Yi Wen:** Writing – original draft, Validation, Software, Resources, Methodology, Investigation, Formal analysis, Data curation, Conceptualization. **Xingkun Xu:** Writing – original draft, Visualization, Resources, Methodology, Investigation, Formal analysis, Data curation, Conceptualization. **Takuji Waseda:** Supervision, Resources, Conceptualization. **Pengzhi Lin:** Supervision, Methodology, Conceptualization.

## Declaration of competing interest

The authors declare that they have no known competing financial interests or personal relationships that could have appeared to influence the work reported in this paper.

## Data availability

The data that supports the findings of this study is partly available online. In particular, the trajectory and intensity of typhoons from the China Meteorological Administration are available at <https://typhoon.weather.com.cn/>. The fifth-generation ECMWF reanalysis for global climate and weather reanalysis data is available at <https://cds.climate.copernicus.eu/cdsapp#!/dataset/reanalysis-era5-single-levels?tab=form>. The validation data for wind, wave, and water level will be made available on request.

## Acknowledgment

This study has been conducted under the support, in part, by the NSFC grant (52031002) and the CSC grant (CSC202106240114). The authors appreciate the support of Dr. Yang Jie from Hohai University for providing the observed wind data and wave gauge data at WG2.

## Appendix A. Supplementary data

Supplementary data to this article can be found online at <https://doi.org/10.1016/j.oceaneng.2024.117683>.

## References

(C3S) CCCS, 2017. ERA5: Fifth Generation of ECMWF Atmospheric Reanalyses of the Global Climate. Copernicus Climate Change Service Climate Data Store (CDS).

- Chen, W.B., 2024. Analysing seven decades of global wave power trends: the impact of prolonged ocean warming. *Appl. Energy* 356, 122440. <https://doi.org/10.1016/j.apenergy.2023.122440>.
- Chen, C., Beardsley, R.C., Cowles, G., Qi, J., Lai, Z., Gao, G., et al., 2011. An unstructured-grid, finite-volume community ocean model. *FVCOM User Manual* 1–409.
- Chen, C., Lao, Q., Zhou, X., Jin, G., Zhu, Q., Chen, F., 2024. Tracks of typhoon movement (left and right sides) control marine dynamics and eco-environment in the coastal bays after typhoons: a case study in Zhanjiang Bay. *Sci. Total Environ.* 912, 168944. <https://doi.org/10.1016/j.scitotenv.2023.168944>.
- CISL RDA. NCEP GFS 0.25 degree global forecast grids historical archive. <https://rda.ucar.edu/datasets/ds084.1/#/description>. (Accessed 22 September 2022).
- CycWEC. <https://atargis.com/index.html>. (Accessed 22 November 2022).
- Dudhia, J., 1996. A multi-layer soil temperature model for MM5. Prepr from Sixth PSU/NCAR Mesoscale Model Users 49–50. Work 22–24 July 1996, Boulder, Color.
- Dyer, A.J., Hicks, B.B., 1970. Flux-gradient relationships in the constant flux layer. *Q. J. Meteorol. Soc.* 96, 715–721. <https://doi.org/10.1002/qj.49709641012>.
- GEBCO. <https://download.gebco.net/>. (Accessed 26 February 2022).
- Harper, P., Hallett, S., Fleming, A., Dawson, M., 2016. 9 - advanced fibre-reinforced composites for marine renewable energy devices. In: Graham-Jones, J., Summerscales, J. (Eds.), *Woodhead Publ. Ser. Compos. Sci. Eng.* Woodhead Publishing. pp. 217–232. <https://doi.org/10.1016/B978-1-78242-250-1.00009-0>.
- Hasselmann, K., Holthuijsen, L.H., Resio, D.T., Westerink, J.J., Maza, M., Lara, J.L., et al., 1973. Measurements of wind-wave growth and swell decay during the joint North Sea wave project (JONSWAP). *Ergänzungsh. Zur Dtsch Hydrogr Zeitschrift* 7.
- Hersbach, H., Bell, B., Berrisford, P., Hirahara, S., Horányi, A., Muñoz-Sabater, J., et al., 2020. The ERA5 global reanalysis. *Q. J. R. Meteorol. Soc.* 146, 1999–2049. <https://doi.org/10.1002/QJ.3803>.
- Hong, S.-Y., Dudhia, J., Chen, S.-H., 2004. A revised approach to ice microphysical processes for the bulk parameterization of clouds and precipitation. *Mon. Weather Rev.* 132, 103–120. [https://doi.org/10.1175/1520-0493\(2004\)132<0103:ARATIM>2.0.CO;2](https://doi.org/10.1175/1520-0493(2004)132<0103:ARATIM>2.0.CO;2).
- Hong, S.-Y., Noh, Y., Dudhia, J., 2006. A new vertical diffusion package with an explicit treatment of entrainment processes. *Mon. Weather Rev.* 134, 2318–2341. <https://doi.org/10.1175/MWR3199.1>.
- Hou, W., Zhang, R., Zhang, P., Xi, Y., Ma, Q., 2021. Wave characteristics and berthing capacity evaluation of the offshore fishing port under the influence of typhoons. *Appl. Ocean Res.* 106, 102447. <https://doi.org/10.1016/j.apor.2020.102447>.
- Huang, J., Hu, X., Ding, J., Gui, J., Zhang, R., 2023. Berthing capacity evaluation of fishing port prone to typhoons: a case study of Shengsi fishing port. *J. Waterw. Port, Coastal, Ocean Eng.* 149, 1–12. <https://doi.org/10.1061/JWPED5.WWENG-1913>.
- Iacono, M.J., Delamere, J.S., Mlawer, E.J., Shephard, M.W., Clough, S.A., Collins, W.D., 2008. Radiative forcing by long-lived greenhouse gases: calculations with the AER radiative transfer models. *J. Geophys. Res. Atmos.* 113, 2–9. <https://doi.org/10.1029/2008JD009944>.
- IEA-OES, 2022. Annual Report: an Overview of Ocean Energy Activities in 2021, p. 220.
- Japan Meteorological Agency. [https://www.jma.go.jp/jma/jma-eng/jma-center/rsmc-hp-pub-eg/besttrack\\_viewer.html](https://www.jma.go.jp/jma/jma-eng/jma-center/rsmc-hp-pub-eg/besttrack_viewer.html). (Accessed 13 February 2023).
- Joint Typhoon warning center. <https://www.metoc.navy.mil/jtvc/jtvc.html>. (Accessed 14 February 2023).
- Kamranzad, B., Lin, P., Wen, Y., 2020. Sustainability of wave energy resources in the South China Sea based on five decades of changing climate. *Energy* 210, 118604. <https://doi.org/10.1016/j.energy.2020.118604>.
- Kamranzad, B., Lin, P., Iglesias, G., 2021. Combining methodologies on the impact of inter and intra-annual variation of wave energy on selection of suitable location and technology. *Renew. Energy* 172, 697–713. <https://doi.org/10.1016/j.renene.2021.03.062>.
- Li, A., Guan, S., Mo, D., Hou, Y., Hong, X., Liu, Z., 2020. Modeling wave effects on storm surge from different typhoon intensities and sizes in the South China Sea. *Estuar. Coast Shelf Sci.* 235, 106551. <https://doi.org/10.1016/j.ecss.2019.106551>.
- Li, J., Pan, S., Chen, Y., Yao, Y., Xu, C., 2022. Assessment of combined wind and wave energy in the tropical cyclone affected region: An application in China seas. *Energy* 260, 125020. <https://doi.org/10.1016/j.energy.2022.125020>.
- Liu, J., Chen, W., Li, J., Sun, L., Li, B., Shi, P., 2022. Observed wave energy variations in coastal regions of the northern South China Sea during Typhoon Lupit (2021). *Energy Rep.* 8, 240–248. <https://doi.org/10.1016/j.egyr.2022.05.092>.
- Loy, K.C., Sinha, P.C., Liew, J., Tangang, F., Husain, M.L., 2014. Modeling storm surges associated with super typhoon durian in South China Sea, 23–37. <https://doi.org/10.1007/s11069-010-9674-7>.
- Macau Meteorological and Geophysical Bureau. <https://www.smg.gov.mo/zh>. (Accessed 26 February 2024).
- OSU TPXO. <https://www.tpxo.net/otps>. (Accessed 26 February 2022).
- P Patel, R., Nagababu, G., Kachhwaha, S.S., V V Arun Kumar, S., M, S., 2022. Combined wind and wave resource assessment and energy extraction along the Indian coast. *Renew. Energy* 195, 931–945. <https://doi.org/10.1016/j.renene.2022.06.082>.
- Paulson, C.A., 1970. The mathematical representation of wind speed and temperature profiles in the unstable atmospheric surface layer. *J. Appl. Meteorol. Climatol.* 9, 857–861. [https://doi.org/10.1175/1520-0450\(1970\)009<0857:TMROWS>2.0.CO;2](https://doi.org/10.1175/1520-0450(1970)009<0857:TMROWS>2.0.CO;2).
- Penalba, M., Ulazia, A., Saénz, J., Ringwood, J.V., 2020. Impact of long-term resource variations on wave energy farms: the Icelandic case. *Energy* 192. <https://doi.org/10.1016/j.energy.2019.116609>.
- Qi, J., Chen, C., Beardsley, R.C., Perrie, W., Cowles, G.W., Lai, Z., 2009. An unstructured-grid finite-volume surface wave model (FVCOM-SWAVE): implementation, validations and applications. *Ocean Model.* 28, 153–166. <https://doi.org/10.1016/j.ocemod.2009.01.007>.
- Seapower. <http://www.seapower.ie/>. (Accessed 17 November 2022).
- Shih, H.J., Chang, C.H., Chen, W.B., Lin, L.Y., 2018. Identifying the optimal offshore areas for wave energy converter deployments in Taiwanese waters based on 12-year model hindcasts. *Energies* 11. <https://doi.org/10.3390/en11030499>.
- Shoreline/coastline databases | NCEI. <https://www.ngdc.noaa.gov/mgg/shorelines/shorelines.html>. (Accessed 10 May 2022).
- Skamarock, William C., Klemp, Joseph B., Dudhia, Jimy, Gill, David O., Barker, Dale M., Duda, Michael G., Huang, Xiang-Yu, Wei Wang, J.G.P., 2008. A description of the advanced research WRF version 3. <https://doi.org/10.1080/07377366.2001.10400427>.
- Su, W.R., Chen, H., Chen, W.B., Chang, C.H., Lin, L.Y., Jang, J.H., et al., 2018. Numerical investigation of wave energy resources and hotspots in the surrounding waters of Taiwan. *Renew. Energy* 118, 814–824. <https://doi.org/10.1016/j.renene.2017.11.080>.
- Sun, Y., Wang, K., Zhong, X., Zhou, Z., Ren, Z., Zhang, J., 2021. Assess the typhoon-driven extreme wave conditions in Manila Bay through numerical simulation and statistical analysis. *Appl. Ocean Res.* 109, 102565. <https://doi.org/10.1016/j.apor.2021.102565>.
- Walsh, K.J.E., McBride, J.L., Klotzbach, P.J., Balachandran, S., Camargo, S.J., Holland, G., et al., 2016. Tropical Cyclones and Climate Change, vol. 7. Wiley Interdiscip Rev Clim Chang, pp. 65–89. <https://doi.org/10.1002/wcc.371>.
- Wang, X., Jin, X., Jia, J., Xia, X., Ping, Y., Gao, J., 2016. Simulation of water surge processes and analysis of water surge bearing capacity in Boao Bay, Hainan Island, China. *Ocean Eng.* 125, 51–59. <https://doi.org/10.1016/j.oceaneng.2016.07.053>.
- Wavestar. <http://wavestarenergy.com/>. (Accessed 17 November 2022).
- Weather China. <http://typhoon.weather.com.cn/>. (Accessed 24 May 2023).
- Webb, E.K., 1970. Profile relationships: the log-linear range, and extension to strong stability. *Q. J. R. Meteorol. Soc.* 96, 67–90. <https://doi.org/10.1002/qj.49709640708>.
- Wei, Y.-M., Chen, K., Kang, J.-N., Chen, W., Wang, X.-Y., Zhang, X., 2022. Policy and management of carbon peaking and carbon neutrality: a literature review. *Engineering*. <https://doi.org/10.1016/j.jeng.2021.12.018>.
- Wen, Y., Kamranzad, B., Lin, P., 2021. Assessment of long-term offshore wind energy potential in the south and southeast coasts of China based on a 55-year dataset. *Energy* 224, 120225. <https://doi.org/10.1016/j.energy.2021.120225>.
- Wen, Y., Kamranzad, B., Lin, P., 2022. Joint exploitation potential of offshore wind and wave energy along the south and southeast coasts of China. *Energy* 249, 123710. <https://doi.org/10.1016/j.energy.2022.123710>.
- Wind power. [https://www.thewindpower.net/store\\_actor\\_en.php?id\\_type=5](https://www.thewindpower.net/store_actor_en.php?id_type=5). (Accessed 15 November 2022).
- Wu, S., Liu, C., Chen, X., 2015. Offshore wave energy resource assessment in the East China Sea. *Renew. Energy* 76, 628–636. <https://doi.org/10.1016/j.renene.2014.11.054>.
- Xu, X., Voermans, J.J., Moon, I.-J., Liu, Q., Guan, C., Babanin, A.V., 2022. Sea spray impacts on tropical cyclone Olwyn using a coupled atmosphere-ocean-wave model. *J. Geophys. Res. Ocean* 127, e2022JC018557. <https://doi.org/10.1029/2022JC018557>.
- Yang, J., Li, L., Zhao, K., Wang, P., Wang, D., Sou, I.M., et al., 2019. A comparative study of typhoon Hato (2017) and typhoon Mangkhut (2018)—their impacts on coastal inundation in Macau. *J. Geophys. Res. Ocean* 124, 9590–9619. <https://doi.org/10.1029/2019JC015249>.
- Yao, C., 2021. Increased Severe Landfall Typhoons in China since 2004, vol. 41, pp. 1018–1027. <https://doi.org/10.1002/joc.6746>.
- Yoshida, K., Sugi, M., Mizuta, R., Murakami, H., Ishii, M., 2017. Future changes in tropical cyclone activity in high-resolution large-ensemble simulations. *Geophys. Res. Lett.* 44, 9910–9917. <https://doi.org/10.1002/2017GL075058>.